PRECISION STRUCTURE FUNCTION MEASUREMENTS FROM CCFR/NUTEV

Janet Conrad
Columbia University
New York, NY 10027

ABSTRACT

New results from the CCFR Collaboration on the structure functions F_2 and xF_3 are presented. Neutrino scattering structure function measurements offer a unique tool to probe the strong interactions. The parity-violating structure function $xF_3(x, Q^2)$ can only be measured in deep inelastic neutrino scattering. Precise measurements of the structure function $F_2(x, Q^2)$ can also be obtained. The predicted Q^2 evolution of these structure functions can be used to test perturbative Quantum Chromodynamics as well as to measure the strong coupling constant, α_s , and the valence, sea, and gluon parton distributions.

1 Introduction

My talk at the 1996 SLAC Summer Institute reviewed many recent QCD results from the Fermilab deep inelastic scattering muon experiment, E665, and neutrino experiment, CCFR. From E665, the analyses included a measurement of the structure function F_2 at very low x (Ref. 1), the ratio F_2^n/F_2^p (Ref. 2), and a measurement of $xG(x,Q^2)$ from hadronic energy flow.[3] The new results of CCFR included presentation of neutrino differential cross sections,[4] a measurement of the structure function $R(x,Q^2)$ (Ref. 4) and a reanalysis of the data to obtain the structure functions $xF_3(x,Q^2)$ and $F_2(x,Q^2)$. Of these many topics, the reanalysis of $xF_3(x,Q^2)$ and $F_2(x,Q^2)$ from CCFR is the most recent result. As such, it is the one analysis that has not yet been described in detail in conference proceedings or papers. Therefore, this paper will concentrate on this new CCFR result. More information on this analysis can be found in the thesis of William Seligman, Columbia University.[5] A publication will be submitted to PRL by the CCFR Collaboration in the near future.

2 Deep Inelastic Neutrino Scattering

The precision measurements of nucleon structure, as probed by neutrino scattering, are interesting as universal, fundamental measurements, as tests of QCD, and as constraints on the parton distributions of the nucleon. Deep inelastic neutrino scattering experiments provide an opportunity to test QCD evolution and extract the QCD parameter Λ, which sets the scale of the strong interaction. In the kinematic regions where the structure of the nucleon can be interpreted in terms of quarks, neutrino scattering has a high sensitivity to many individual parton distributions. Probing the nucleon with neutrinos is complementary to charged lepton scattering experiments. Comparisons between neutrino and charged lepton deep inelastic experiments test the universality of the structure functions and parton distributions. Global analyses which include all of the neutrino data provide the best parametrizations of the individual parton distributions.

Because the topic of this summer school was QCD studies, familiarity with the ideas of QCD is assumed. This section provides a very brief introduction to deep inelastic neutrino scattering.

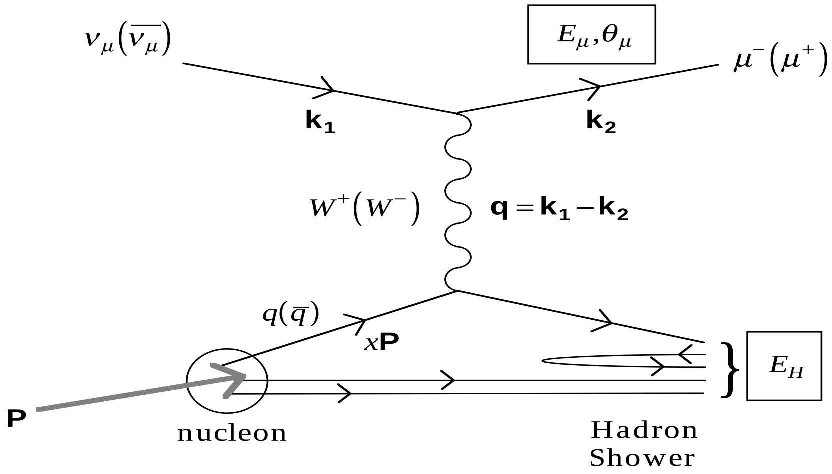

Figure 1: The first-order feynman diagram for deep inelastic neutrino scattering.

2.1 Kinematics of Deep Inelastic Scattering (DIS)

The tree-level diagram for charged current neutrino-nucleon scattering is shown in Fig. 1. A neutrino (antineutrino) with incoming four-momentum, k_1, scatters from a quark or antiquark in the nucleon via exchange of a W^+ (W^-) boson, with four-momentum q. In the lab, the variables which can be measured in this interaction are the momentum and angle of the outgoing muon, E_μ and θ_μ, and the energy of the outgoing hadrons E_{had}. These can be used to reconstruct the energy of the incoming neutrino, $E_\nu = E_\mu + E_{had}$. In terms of these variables, the four-vectors shown in Fig. 1 are:

$$\begin{aligned} k_1 &= (E_\nu, 0, 0, E_\nu) \\ k_2 &= (E_\mu, p_\mu \sin\theta_\mu \cos\phi_\mu, p_\mu \sin\theta_\mu \sin\phi_\mu, p_\mu \cos\theta_\mu) \\ p &= (M, 0, 0, 0) \\ q &= k_1 - k_2. \end{aligned}$$

Useful invariant quantities which describe the interaction are:

$$\begin{aligned} Energy\ transfer : \nu = (p \cdot q)/M \\ Fractional\ Energy\ Transfer : y = M\nu/p \cdot k_1 \\ Negative\ Squared\ 4 - Momentum : Q^2 = -q^2 \\ The\ Bjorken\ Scaling\ Variable : x = Q^2/(2p \cdot q). \end{aligned}$$

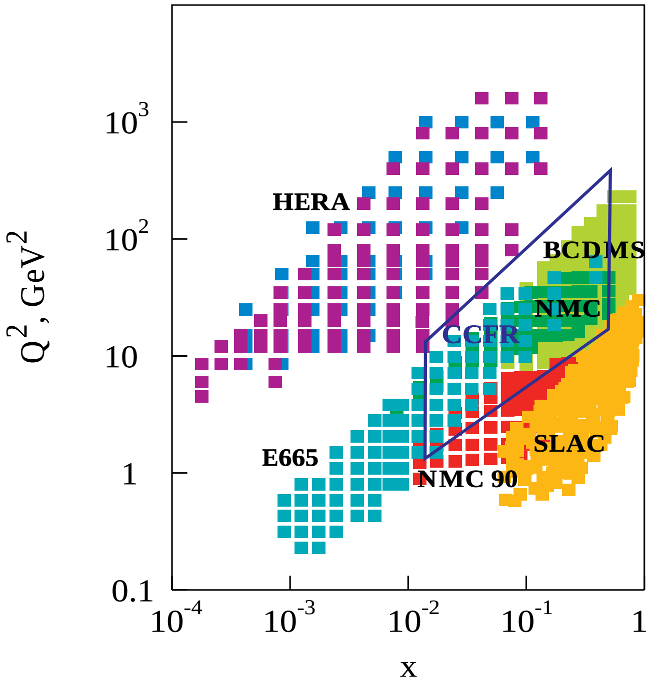

Figure 2: The kinematic region accessible to the CCFR experiment (solid outline) and other deep inelastic scattering experiments.

In the lab frame, these reduce to:

$$\nu = (E_\nu - E_\mu) = E_{had} - M \tag{1}$$

$$y = \nu / E_\nu \tag{2}$$

$$Q^2 = m_\mu^2 + 2E_\nu(E_\mu - p_\mu \cos\theta_\mu) \tag{3}$$

$$x = Q^2/(2M\nu). \tag{4}$$

For a given beam energy, E_ν, the accessible kinematic region is, in principle, bounded by:

$$\begin{aligned} 0 \leq\ & \nu \leq E_\nu \\ 0 \leq\ & y \leq 1 \\ 0 \leq\ & Q^2 \leq 2ME_\nu \\ 0 \leq\ & x \leq 1. \end{aligned}$$

In practice, experimental cuts to isolate regions of high acceptance and small corrections may reduce the available range. The accessible kinematic range can be described in the plane of any two of the above variables. The wide band beam of CCFR extended up to 600 GeV and the resulting kinematic range in the x and Q^2 plane is shown in Fig. 2 in comparison to other deep inelastic scattering experiments.

2.2 The Neutrino-Nucleon Cross Section and the Structure Functions

The general form for the differential cross section depends upon three structure functions, F_2, R, and xF_3:

$$\begin{aligned}\frac{d^2\sigma^{\nu(\overline{\nu})}}{dxdy} &= \frac{G_F^2 M E_\nu}{\pi(1+Q^2/M_W^2)^2}\left[F_2^{\nu(\overline{\nu})}\left(\frac{y^2+(2Mxy/Q)^2}{2+2R^{\nu(\overline{\nu})}}+1-y-\frac{Mxy}{2E_\nu}\right)\right.\\ &\left.\pm xF_3^{\nu(\overline{\nu})}y\left(1-\frac{y}{2}\right)\right]. \qquad (5)\end{aligned}$$

The structure functions depend upon the kinematic variables x and Q^2. The functions F_2 and R are also measured in deep inelastic charged lepton scattering. R can be interpreted as the ratio of the longitudinal to transverse virtual boson absorption crosssection. The function xF_3 appears only in the cross section for the weak interaction. It is derived from the parity-violating term in the product of the leptonic and hadronic tensor.

In the parton model, the neutrino structure functions can be written as functions of the sums and differences of the quark probability distributions. The probability of scattering from a parton with a given fractional momentum x is represented by the quark probability distribution. The structure functions depend on the quark distributions weighted by the fractional momentum and by the squared charge of the quarks, which is unity in the weak interaction. The quark probabilities are related to xF_3 by:

$$xF_3 = x(\sum_i q_i(x) - \overline{q}_i(x)) = x(u_v + d_v), \qquad (6)$$

where u_v and d_v are the valence quark distributions. The structure function F_2 is given by:

$$F_2 = x(\sum_i q_i(x) + \overline{q}_i(x)). \qquad (7)$$

Within QCD, low transverse momentum quark-gluon interactions may occur at the time of the scatter. Thus, partons with higher fractional momentum may contribute to interactions at any lower x through radiation or gluon splitting. The probability that the interaction resolves such a splitting depends on Q^2. This splitting modifies the structure functions, leading to a Q^2 dependence known as scaling violations. The QCD Dokshitser–Gribov–Lipatov–Altarelli–Parisi (DGLAP) equations[6] predict the Q^2 dependence of the structure functions and underlying parton distributions.

From the DGLAP equations, the change in the structure functions with Q^2 as a function of x depends on α_s. At next-to-leading order, α_S is given by:

$$\alpha_S(Q^2) = \frac{4\pi}{\beta_0 \ln(Q^2/\Lambda^2)}[1 - \frac{\beta_1}{\beta_0}\frac{\ln[\ln(Q^2/\Lambda^2)]}{\ln(Q^2/\Lambda^2)}], \tag{8}$$

where $\beta_0 = 11 - 2n_f/3$ and $\beta_1 = 102 - 38n_f/3$, and n_f is the number of quark flavors participating in the interaction at this Q^2. The QCD coupling constant, Λ, must be introduced when the renormalization technique is applied to remove the divergences within QCD. In this analysis, the modified minimal subtraction scheme ($\overline{MS}$) scheme is used.

2.3 Nonperturbative QCD and Nuclear Effects

Nonperturbative QCD processes which might affect the CCFR structure function measurements are collectively termed higher twist effects. These effects occur at low Q^2 where the impulse approximation of scattering from massless non-interacting quarks is no longer valid. Examples include the target mass effects, diquark scattering, and other multiparton effects. The functional form for target mass effects has been determined.[7] The remaining higher twist effects cannot be calculated a priori, but must be measured. A measurement of the contribution of the higher twist terms in charged lepton scattering was made by comparing the SLAC and BCDMS F_2 data to the QCD expectation.[8] Deviations were attributed entirely to higher twist effects and were fit to the form: $F_2^{Measured}/F_2^{predicted} = (1 + C_i/Q^2)$. Separate constants, C_i, were calculated for each x bin. For the CCFR analysis presented below, it was assumed that the measured corrections are applicable to both F_2 and xF_3 in neutrino scattering.

The results presented here are structure functions for neutrino nucleon scattering on iron. The data were corrected to an isoscalar target, but not for nuclear effects. High x bins are expected to be affected by Fermi smearing, and therefore are not included in the fits used to extract the parton distributions and α_s.

2.4 Measurement of the Strange Sea

The flavor-changing quality of the weak interaction allows for the opportunity to directly tag scattering from specific quark flavors. In particular, charged current scattering from strange quarks has the distinct experimental signature of producing two muons of opposite sign, one from the scattered lepton and the other from the semileptonic decay of the produced charm. The strange sea is described by the functions:

$$\begin{aligned} xs(x) &= A_s(1-x)^\alpha[x\overline{u}(x)+\overline{d}(x)]/2 && (9) \\ \kappa &= (\int_0^1 dx[xs(x)+\overline{s}(x)])/(\int_0^1 dx[x\overline{u}(x)+\overline{d}(x)]) && (10) \\ A_s &= \kappa\int_0^1 dx\frac{x\overline{q}(x,Q^2)}{2+A_s(1-x)^\alpha}/\int_0^1 dx\frac{(1-x)^\alpha x\overline{q}(x,Q^2)}{2+A_s(1-x)^\alpha}, && (11) \end{aligned}$$

thus, α represents the relative shape and κ gives the overall normalization relative to the nonstrange sea. The equation for A_S, which relates κ and α, must be solved numerically.

The best measurement to date has come from the dimuon studies of the CCFR Collaboration, where the next-to-leading-order analysis has yielded $\alpha = -0.05 \pm 0.56 \pm 0.10$ and $\kappa = 0.468^{+0.064-0.017}_{-0.051+0.036}$ (Ref. 9). The results of the CCFR measurements at leading and next-to-leading order are used in the analysis described below.

3 The CCFR and NuTeV Experiments

The data presented in this paper were taken by the CCFR Collaboration during the 1985 and 1987 fixed-target runs at Fermilab. The CCFR neutrino beam resulted from decays of pions and kaons produced in interactions of the 800 GeV FNAL proton beam with a beryllium target. This wide-band beam ranged in energy up to 600 GeV and resulted in events of which 86.4% were due to ν_μ's, 11.3% $\overline{\nu}_\mu$'s, and 2.3% ν_e's and $\overline{\nu}_e$'s. Neutrino events were observed in the Lab E neutrino detector,[10] shown in Fig. 3, which consists of a target calorimeter followed by a toroid muon spectrometer. The calorimeter consists of 84 3 m × 3 m × 10 cm iron plates, interspersed with scintillators for energy measurement and drift chambers for muon tracking. The toroid spectrometer has five sets of drift chambers for muon tracking as well as hodoscopes for triggering. For the CCFR experiment,

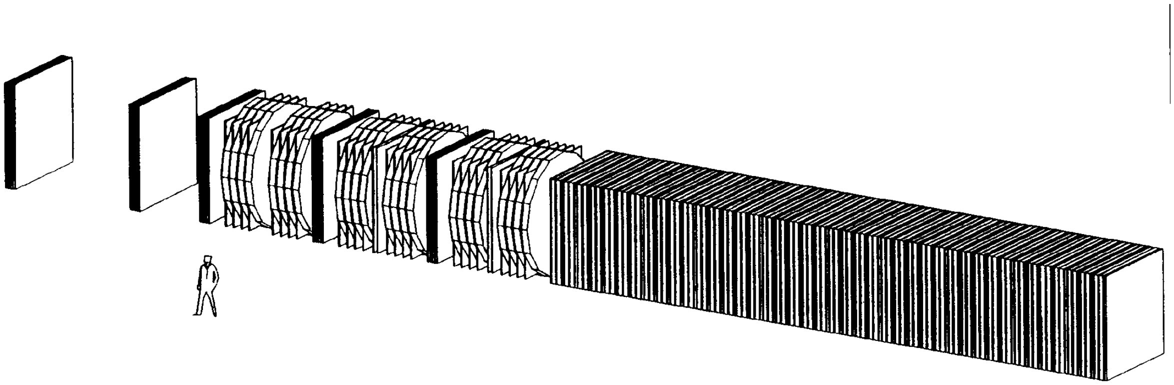

Figure 3: The Lab E neutrino detector.

the detector was calibrated during special runs using a test beam of pions, electrons, and muons. Details of the CCFR beam and detector can be found in Ref. 10.

NuTeV, the next generation of deep inelastic neutrino scattering experiments at Fermilab, began taking data in May 1996. NuTeV has modified the beamline to select the sign of the charged pions and kaons.[11] The resulting beam is almost purely ν_μ or $\overline{\nu}_\mu$, depending on the sign selection. An increase in the antineutrino-to-neutrino ratio over CCFR will improve several of the QCD measurements. The sign selection also will allow new QCD studies. Separate running will also permit the first high-statistics simultaneous measurements of the electroweak mixing parameter, $\sin^2\theta_W$, and neutral to charged current coupling strength ratio, ρ. The Lab E neutrino detector is being used, after substantial upgrades. To improve sensitivity to a single minimum ionizing particle, we have replaced the scintillator oil and phototubes of the scintillation counters. The drift chambers have been fully refurbished and the TDC/DAQ system has been upgraded. At NuTeV, the detector is calibrated with a test beam of pions, electrons, or muons continuously throughout the running. The new test beam also provides a broader range of hadron and muon energies than the CCFR test beam.

4 The Measurement of the Neutrino Flux

In the analysis described below, the low ν (*i.e.,* low E_{had}) data are used to determine the flux of the incoming neutrinos and anitneutrinos. The kinematic cuts on the data used to determine the flux are

$$\begin{aligned} \theta_\mu &< 150\ mr \\ E_\mu &> 15\ GeV \\ 30 < E_\nu &< 360\ GeV \\ E_{had} &< 20\ GeV. \end{aligned}$$

These cuts, in combination with fiducial volume cuts, assured good acceptance for the flux extraction events, while having little overlap with the events used to determine the structure functions.

The CCFR flux is obtained from the y dependence of the data. The relationship between the number of observed events, the flux, and the cross section is:

$$\frac{dN_{\nu,\overline{\nu}}}{dy} = \Phi_{\nu,\overline{\nu}}(E)\frac{d\sigma_{\nu,\overline{\nu}}}{dy}. \tag{12}$$

This can be parametrized as a polynomial in terms of $y = \nu/E_\nu$

$$\frac{dN_{\nu,\overline{\nu}}}{d\nu} == A_{\nu,\overline{\nu}} + B_{\nu,\overline{\nu}}(\nu/E_\nu) + (C_{\nu,\overline{\nu}}/2)(\nu/E_\nu)^2. \tag{13}$$

In this case, A, B, and C are:

$$A = \frac{G^2M}{\pi}\int_0^1 F_2(x,Q^2)\Phi(E_\nu)dx \tag{14}$$

$$B = -\frac{G^2M}{\pi}\int_0^1 (F_2(x,Q^2) \mp xF_3(x,Q^2))\Phi(E_\nu)dx \tag{15}$$

$$C = B - \frac{G^2M}{\pi}\int_0^1 F_2(x,Q^2)\tilde{R}(x,Q^2)dx \tag{16}$$

with

$$\tilde{R}(x,Q^2) \equiv \frac{1+2Mx/\nu}{1+R(x,Q^2)} - \frac{Mx}{\nu} - 1. \tag{17}$$

A, B, and C are assumed to be only dependent upon E_ν. Integrating Eq. 12, the number of events for $\nu < \nu_0$ is:

$$N = \Phi(E)\int_0^{\nu_0} d\nu A\left[1 + \frac{\nu}{E_\nu}\frac{B}{A} - \frac{\nu^2}{2E_\nu^2}\left(\frac{B}{A} - \frac{\int F_2\tilde{R}}{\int F_2}\right)\right]. \tag{18}$$

Thus, the flux is obtained by binning events in E_ν and $E_{had} < \nu_0$.

CCFR uses an iterative method to determine the flux. Initially, a parton distribution is input to the Monte Carlo to determine A, B, and C. Then the data in the range $\nu < 20$ GeV are used to determine the flux as a function of energy for neutrinos and antineutrinos separately, up to an overall normalization constant. This flux is then used to extract cross sections using $\nu > 10$ GeV data. Thus, the region of overlap between the data used to determine the flux and that used to determine the cross section is small. The data is normalized to the world–average cross section for νFe, as discussed below. Structure functions are then extracted following the prescription described in the following section. Parameterizations of the structure functions are used as input to Monte Carlo for the next iteration. This algorithm usually converges after the second iteration.

The assumption that the integrals over the structure functions are independent of ν, and thus depend only on E_ν, is only approximately true. Recall that $Q^2 = 2M\nu x$; therefore for fixed ν, using F_2 as an example:

$$\int_0^1 F_2(x,Q^2) = \int_0^1 F_2(x, 2M\nu x) \equiv F_2^{int}(\nu). \qquad (19)$$

The systematic error introduced by this residual ν dependence was studied by varying the ν range from which the flux was extracted. The systematic error from assuming no ν dependence was found to be less than 0.5%.

Because this algorithm determines the relative shape of the flux distribution with energy, but not the overall normalization, the cross section for νFe scattering is an input to the analysis. The world-average neutrino cross section for iron is $\sigma^\nu/E = (0.677 \pm 0.014) \times 10^{-38} cm^2/GeV$ (Ref. 5). While the absolute flux of neutrinos and antineutrinos is not fixed by the CCFR method, the relative neutrino and antineutrino flux in each energy bin is determined. The preliminary ratio of the total cross sections, $\sigma^{\overline{\nu}}/\sigma^\nu$ from the flux extraction method, was found to be 0.509 ± 0.010. The world average including this experiment, which is used to obtain the final relative normalization, is 0.500 ± 0.007. The errors in the averages are included in the systematic error for the determination of the differential cross section and the structure functions.

Figure 4 shows the CCFR flux of neutrinos and antineutrinos.

0bp !

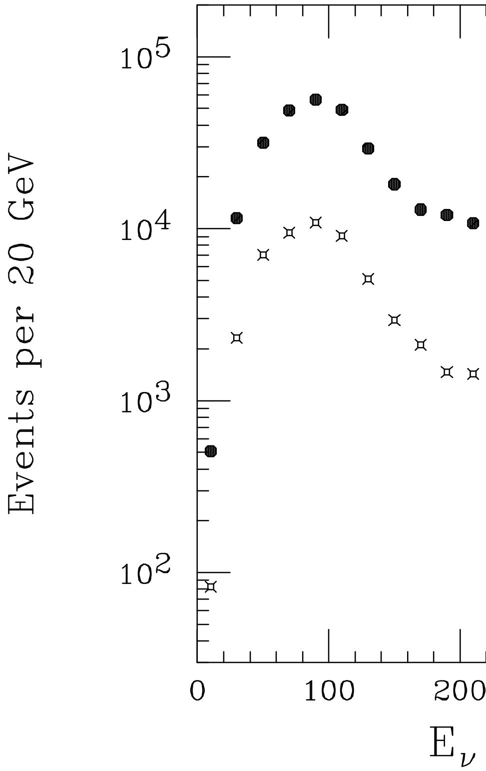

Figure 4: The CCFR neutrino and antineutrino fluxes.

5 The Measurement of F_2 and xF_3

The structure functions F_2 and xF_3 are extracted from the differential cross section given the flux determined by the method described above. The following kinematic cuts were made on the data:

$$\begin{array}{rl} 30 & < E_\nu < 360\ GeV \\ \theta_\mu & < 150\ mr \\ E_\mu & > 15\ GeV \\ Q^2 & > 1\ GeV^2 \\ E_{had} & > 10\ GeV, \end{array}$$

plus fiducial volume cuts, to assure good acceptance. All dimuon events were cut from the sample for two reasons. First, when one muon fails to traverse the toroid, the event could have improperly reconstructed kinematics. Second, at high y, even if both muons traverse the toroid, the algorithm to identify the scattered muon, as versus the charm-decay muon, was not perfectly efficient. The data were corrected for this cut based on the CCFR dimuon measurements discussed above. The data were acceptance corrected. Radiative corrections based on the calculation by Bardin,[12] which includes muon and quark radiation and the box diagram, were applied. Corrections to an isoscalar target and to remove the charm mass and the propagator effects are included to make the comparison to other experiments straightforward. The number of events in each x and Q^2 bin is related to the differential cross section by:

$$N = \rho L N_A \int_{x-bin} \int_{Q^2-bin} \left[\int_{all\ energies} \frac{d^2\sigma}{dx dQ^2} \Phi(E) dE \right], \tag{20}$$

where ρ is the target density, L is the target length, and N_A is Avagadro's number. The structure functions are extracted from these differential cross sections. For this analysis, R was assumed to be given by the parametrization "$R_{\mathrm{W}hitlow}$."[13]

Many sources of systematic error were considered in this analysis. The hadron energy and muon energy are determined by the test beam data and each is estimated to be known to 1%. The statistical error in the flux extraction was typically also on the order of 1%. There is an error of 2.1% associated with the normalization of the cross section to the world's data. Model-dependent systematic errors included a 15% error on the $R_{mathrmWhitlow}$ parametrization, an 18% error on the leading-order charm mass, 26% error on the leading-order strange sea shape, 1.7% on the strange sea normalization, and 7% on the charm branching ratio. Of these sources of systematic error, the calibration errors most strongly affect the QCD analysis.

The data presented here represent a reanalysis of the CCFR data, which differs from the previous analysis[14] in the following ways:

- The hadronic energy and muon calibrations are extracted directly from the test beam data. The previous analysis used a technique of adjusting the measured calibration which was later shown to have large associated systematic uncertainties.
- The muon energy loss in the calorimeter is more accurately modeled in the Monte Carlo simulation of the detector.
- The previously presented data included radiative corrections only for radiation from the muon. The radiative corrections applied to the data presented here also include the contributions from the box diagram.[12]
- The parametrization $R_{Whitlow}$, which is the most inclusive fit to date, is not identical to R_{SLAC}, which was the best parametrization available for the previous analysis.

Detailed information on each of the improvements can be found in Ref. 5.

Figures 5 and 6 show the preliminary CCFR measurements of F_2 and xF_3 as a function of Q^2 in various bins of x. Only statistical errors are shown. The solid and dashed lines on the plot indicate the QCD fits which are discussed in the following section.

When the final results are obtained, the information will be available in tabular form by contacting seligman@nevis1.columbia.edu.

6 QCD Studies and Comparison to Other Experiments

In this section, the preliminary CCFR results are compared to results from other experiments. First, F_2 is compared to that determined by charged lepton deep inelastic scattering. Second, the QCD fits to the CCFR structure functions are described and the extracted value of α_s is compared to the measurements of other

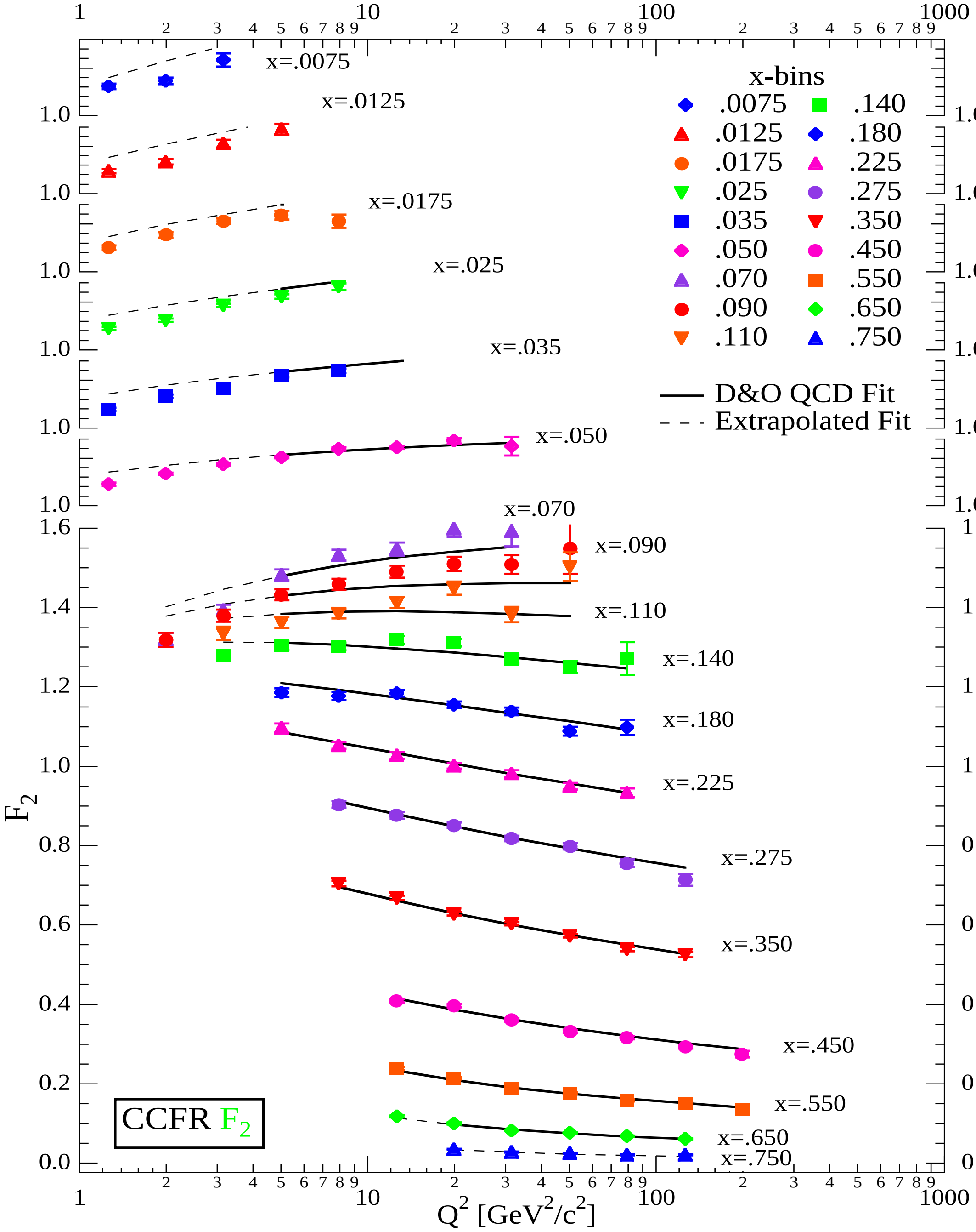

Figure 5: Preliminary CCFR F_2 measurement. Errors are statistical only. Lines indicate the QCD fit discussed in Sec. 6.

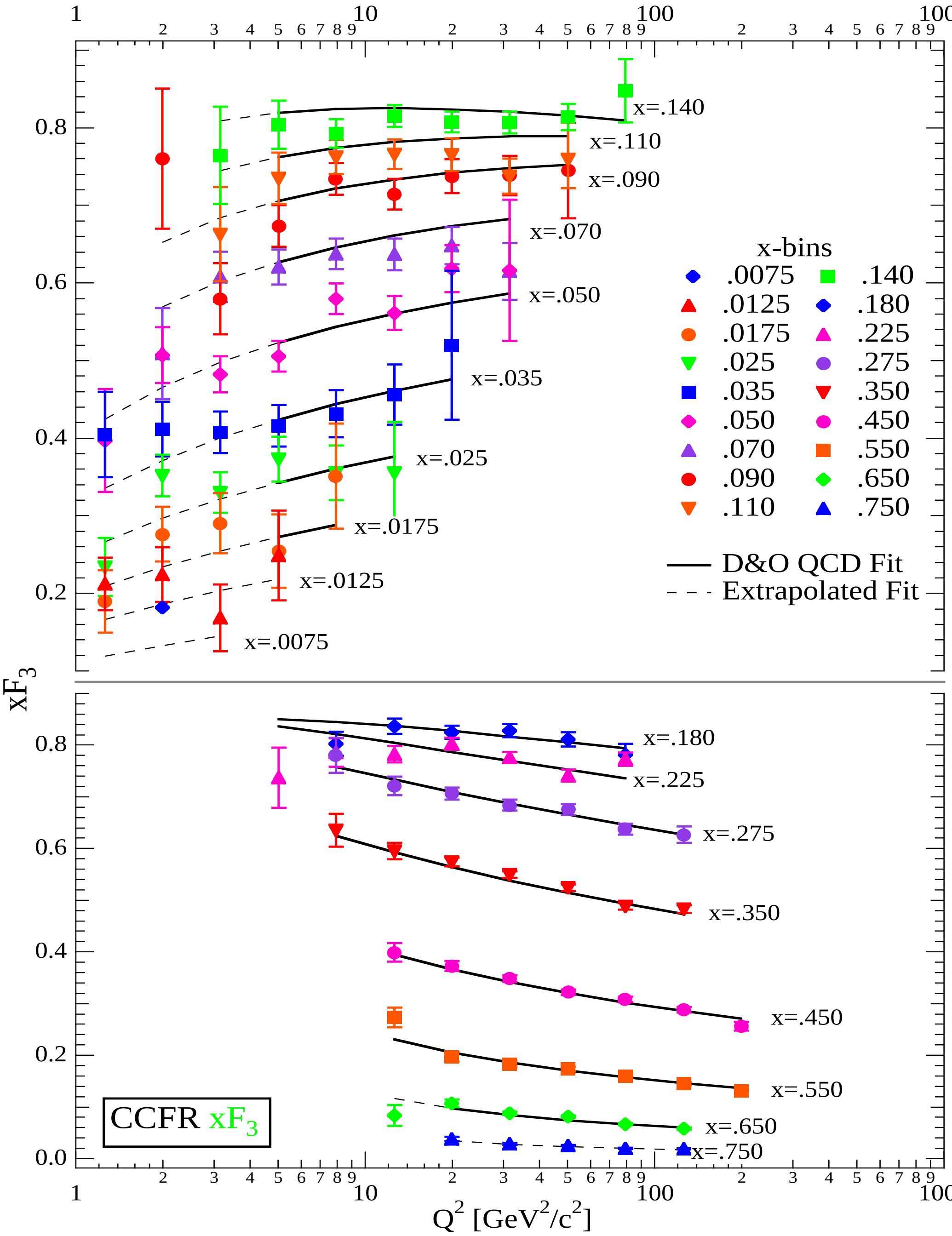

Figure 6: Preliminary CCFR xF_3 measurement. Errors are statistical only. Lines indicate the QCD fit discussed in Sec. 6.

experiments. Finally, the gluon distribution from the CCFR global fit is compared to previous results.

6.1 F_2 from Neutrino and Charged Lepton Scattering

The parity-conserving structure function F_2 is measured by both charged and neutral lepton scattering experiments. The definition of F_2 at lowest order is given by:

$$\sum_i e_i^2 q_i(x) + e_i^2 \overline{q}_i(x), \tag{21}$$

where e_i represents the charge associated with the coupling to each quark type i. In neutrino scattering, the "weak charge" is unity. In the case of muon scattering, the coupling is electromagnetic; hence, the definition of F_2 includes the quark charges squared. As a result of the difference in coupling between the electromagnetic and weak interactions, a conversion must be applied in order to compare muon and neutrino experiments. To lowest order, the correction is:

$$F_2^{\mu} = \frac{5}{18} F_2^{\nu} \left[1 - \frac{3(s+\overline{s})}{5(q+\overline{q})} \right]. \tag{22}$$

The strange sea (s, $\overline{s}$) appears explicitly in this equation. This can be precisely measured by charged-current neutrino scattering from strange quarks producing opposite sign dimuons, as discussed in Sec. 2.4 above. The CCFR next-to-leading-order measurement of the strange sea is used to make the corrections in this discussion.[9]

Nuclear effects must also be considered when comparing muon and neutrino measurements of F_2. Neutrino scattering experiments typically use high-density nuclear targets because the neutrino cross section is very small. The CCFR results were obtained with an iron target (bound nucleons). The electromagnetic cross section is reasonably large, and so muon experiments typically use hydrogen and deuterium (free and loosely bound nucleons, respectively). The difference in F_2 between bound nucleons and free nucleons has been studied in charged lepton experiments. The corrections used below are from a fit to NMC, E665, and SLAC data.[15] The fit is compared to the charged lepton results in Fig. 7.

Figures 8 through 13 compare the preliminary F_2 measured by CCFR and discussed above to the measurements from NMC over a range of x regions.[16] The corrections for charge coupling and nuclear effects have been applied to the muon

10bp !

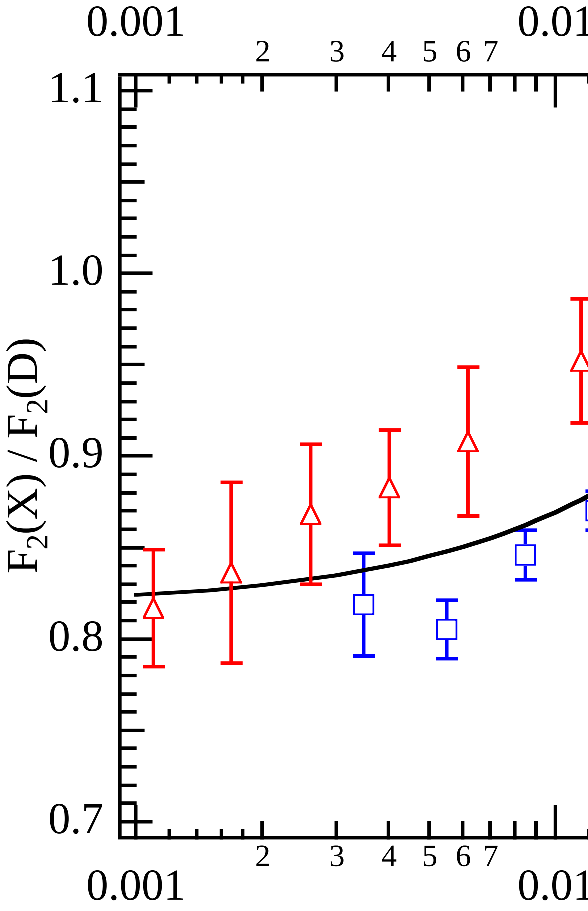

Figure 7: Fit to the NMC, E665, and SLAC nuclear data. The resulting fit is used to correct the charged lepton deuterium data for comparison with the CCFR result.

10bp !

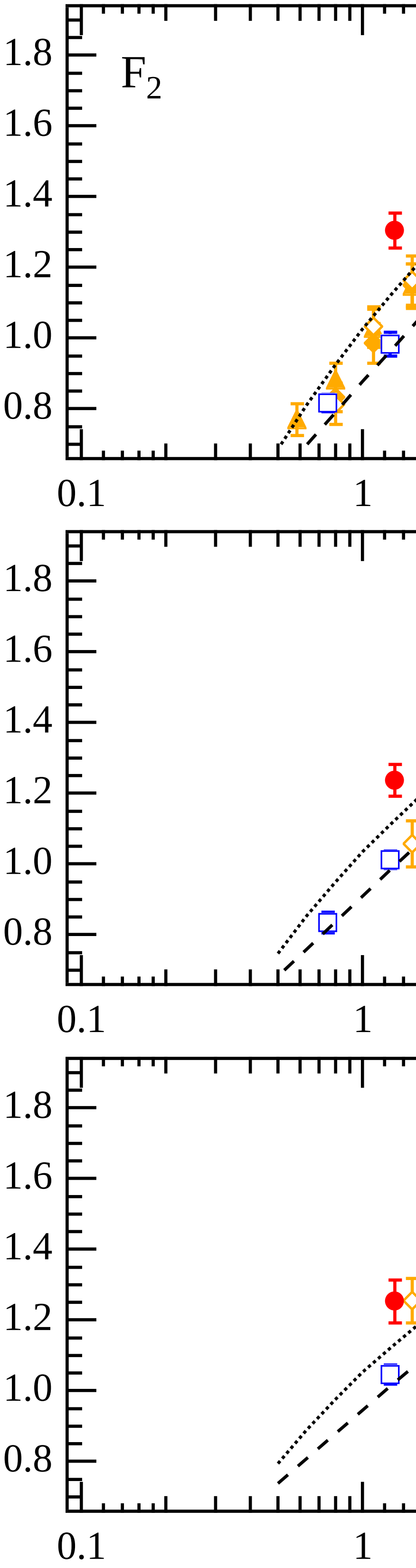

Figure 8: Comparison of the CCFR (ν) measurement of F_2 to the NMC and E665 (μ) results for $x = 0.0075, 0.0125$, and 0.0175. Corrections for definition of F_2 and

10bp !

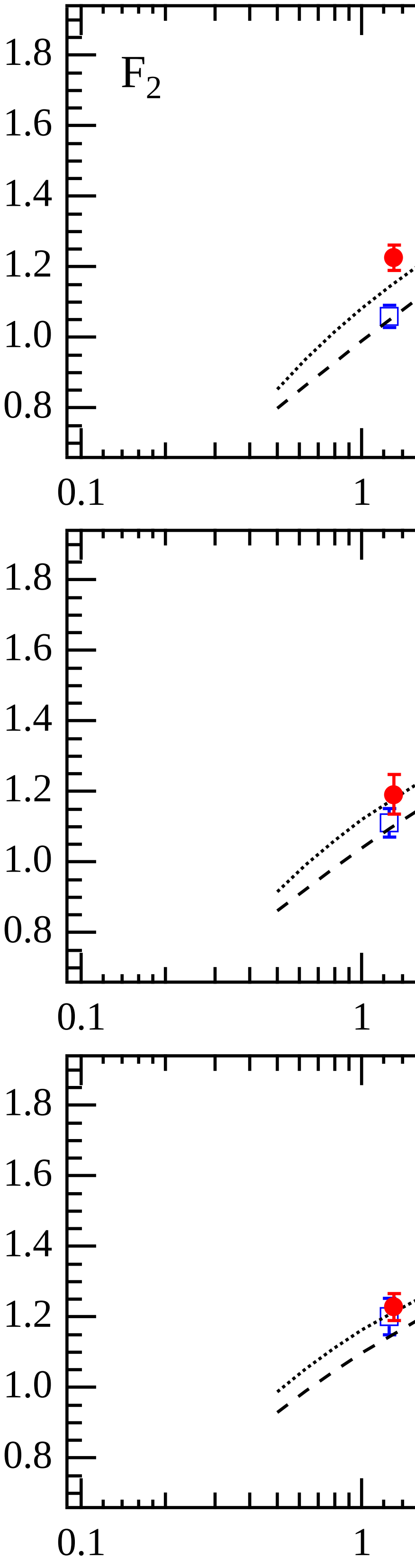

Figure 9: Comparison of the CCFR (ν) measurement of F_2 to the NMC and E665 (μ) results for $x = 0.0250, 0.035$, and 0.050. Corrections for definition of F_2 and

10bp !

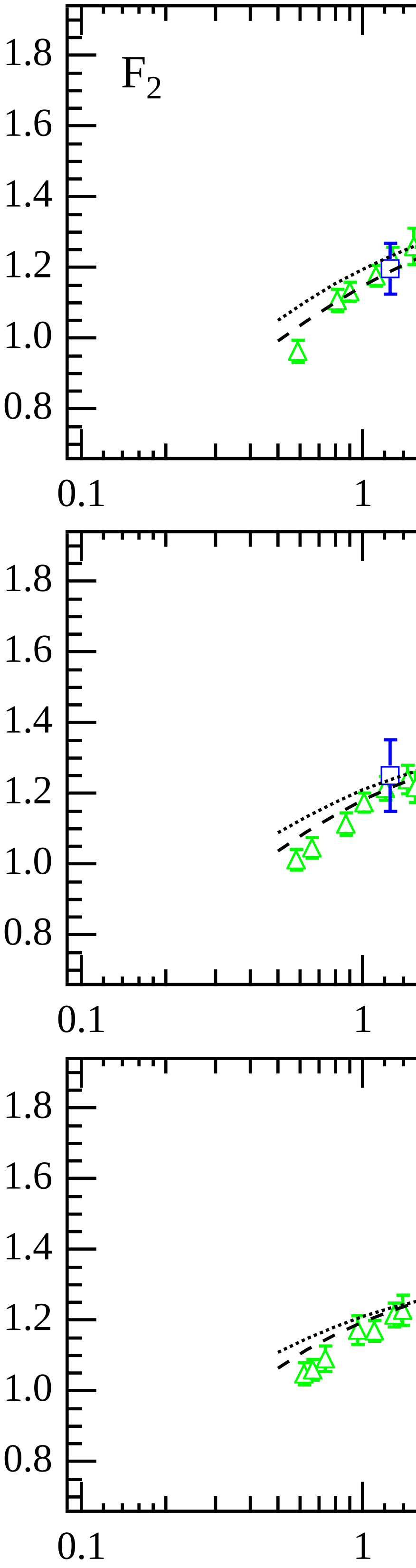

Figure 10: Comparison of the CCFR (ν) measurement of F_2 to the NMC and E665 (μ) results and SLAC (e) results for $x = 0.070, 0.090$, and 0.110. Corrections for

10bp !

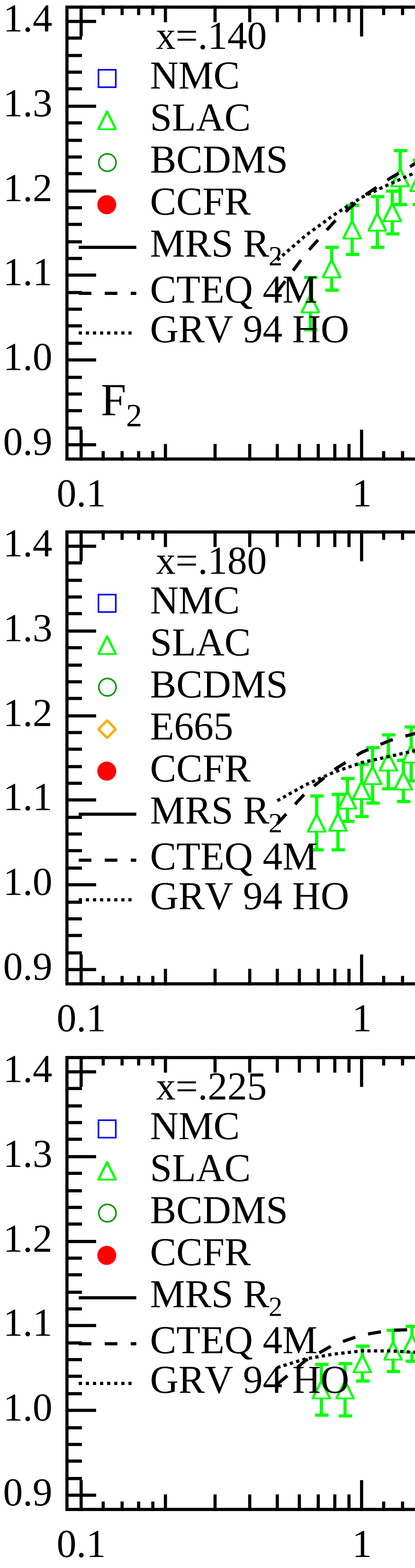

Figure 11: Comparison of the CCFR (ν) measurement of F_2 to the NMC and E665 (μ) results for $x = 0.140, 0.180$, and 0.225. Corrections for definition of F_2 and for

10bp !

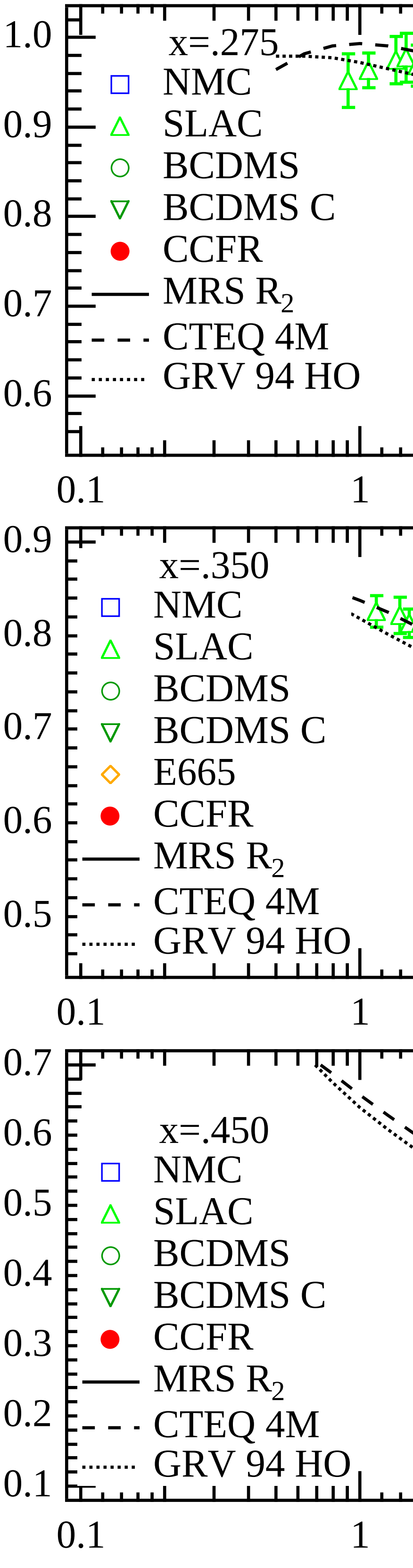

Figure 12: Comparison of the CCFR (ν) measurement of F_2 to the NMC and E665 (μ) results for $x = 0.275, 0.350$, and 0.450. Corrections for definition of F_2 and for

10bp !

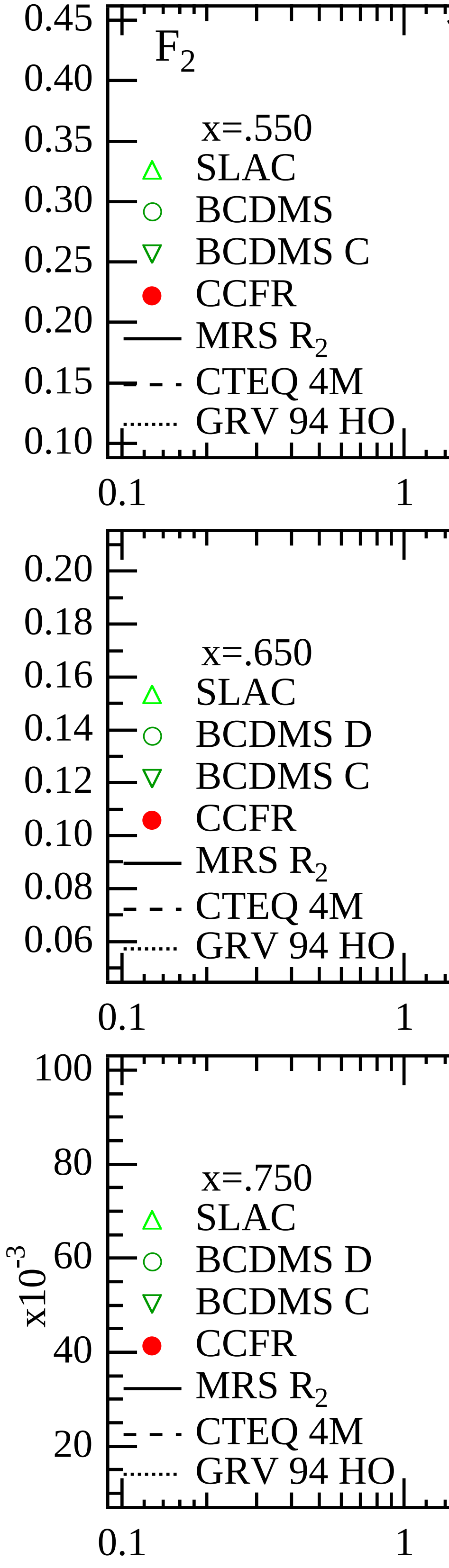

Figure 13: Comparison of the CCFR (ν) measurement of F_2 to the NMC and E665 (μ) results for $x = 0.550, 0.650,$ and 0.750. Corrections for definition of F_2 and for

data. At low x, there appears to be a disagreement between the charged lepton scattering data and the neutrino data. The discrepancy decreases with increasing x until, in the region of $x \approx 0.070$, the data are in good agreement, which continues to the highest x bins.

The high-statistics data in the region of the discrepancy come from CCFR and NMC. It is possible that one or both experiments have underestimated their systematic errors in this region. The most important systematic error in the CCFR analysis is due to the calorimeter calibration. Extensive studies of the test beam data were undertaken in order to determine the muon and hadron energy calibration, and we believe the systematic error assigned to these are conservative.

Another cause for the disagreement may be the nuclear correction applied to the charged lepton deuterium data in order to allow comparison with the neutrino results. This correction assumes that effects in scattering from bound nucleon targets are the same for muons and neutrinos in the low x ("shadowing") region. However, if shadowing effects are caused by fluctuations of the intermediate virtual boson to mesons, then one might expect differences. The vector-meson-dominance model ascribes the cause of shadowing to fluctuations of the vector boson into mesons leading to strong interactions near the "surface" of the nucleon. In the case of muon scattering, the photon can fluctuate only into vector mesons, while for neutrinos, the W has an axial as well as a vector component. Very little data on shadowing in neutrino scattering has been obtained because of the low event rate for neutrinos in a deuterium target. The best measurements come from the BEBC Collaboration on neon vs deuterium, in which shadowing was found to be consistent with that observed in charged lepton scattering in the $x = 0.02$ and $Q^2 > 1.0\ GeV^2$ region.[17]

Although the NMC and E665 shadowing data which were fit to obtain the nuclear correction are in statistical agreement, there appears to be a systematic shift between the two data sets, as can be seen in Fig. 7. The fit is dominated by the NMC result, which has much smaller errors than the E665 data. However, if only the E665 data are used in a fit which is then applied to the charged lepton deuterium results, then the CCFR/NMC discrepancy is reduced by approximately a factor of two for $x < 0.03$.

Several publications have suggested that the discrepancy is due to an incorrect strange sea correction.[19,?,?] The required distributions to eliminate the discrepancy are inconsistent with, and approximately a factor of two larger at, low x than

10bp !

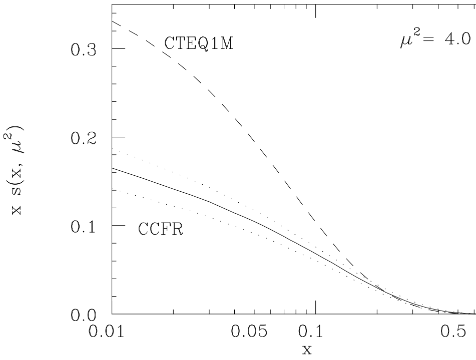

Figure 14: Solid—the strange sea as measured by the CCFR Collaboration from the dimuon data. The surrounding dots show the statistical and systematic errors combined. Dashed—the strange sea required to account for the neutrino-charged-lepton discrepancy, as determined by Ref. 19.

the CCFR measurement from the dimuon data, as calculated at next-to-leading order by the CTEQ Collaboration.[19] The CCFR measurement of the strange sea, which is to next-to-leading order and includes corrections for the charm-mass threshold, would have to be incorrect by 5σ to account for the discrepancy. This is shown in Fig. 14, where the solid line is the CCFR measurement, the dotted lines indicate the 1σ systematic and statistical errors on the CCFR result, and the dashed line shows the magnitude of the strange sea required to explain the discrepancy in the F_2 measurements. In this study, the strange and antistrange sea distributions were assumed to be equal.

Brodsky and Ma have suggested that the strange and antistrange sea distributions may not be equal.[20] If the proton fluctuates into a virtual $K^+\Lambda$ pair, then the s quark becomes a valance quark of the Λ with a relatively harder momentum distribution than the $\overline{s}$ quark. CCFR has measured the strange and antistrange distributions separately using the dimuon data. The scattered muon was identified using a P_T and energy algorithm, as described in Ref. 9. The sign of the scattered and charm-decay muons identified whether the scatter was from s or $\overline{s}$. The data indicated that the distributions were consistent within the statistical and systematic errors. However, the power–law parametrization which was used for the fits is not the same as the distribution predicted by Brodsky and Ma's model. Therefore the asymmetric intrinsic strange sea may be masked by the choice of functional form required by the fit. A reanalysis using the functional form of the model is underway.

In order to fully investigate the discrepancy in the F_2 measurements, more data in the low x region are required. The NuTeV experiment, described above, is expected to obtain approximately equal statistical errors on F_2 with substantially reduced systematics. Precise hadron energy calibration will be obtained with the new continuous test beam over a wider range of energies than those covered by CCFR. Also, NuTeV will provide a more accurate measurement of the strange and antistrange seas. This is because the sign selection of the beamline determines the sign of the scattered muon, allowing accurate identification even when only one of the two muons in a dimuon event reaches the toroid spectrometer. Thus, the statistical sample will be larger, and the systematics due to misidentification will be smaller.

6.2 Measurements of α_s and $\Lambda_{\overline{MS}}$

Perturbative QCD can predict the evolution of the structure functions from a starting set of x-dependent distributions,[6] as described in Sec. 2.2. In this analysis, the QCD parameter is determined to next-to-leading order (NLO) for four flavors in the $\overline{MS}$ renormalization scheme: $\Lambda^{NLO\ 4flv}_{\overline{MS}}$.

The QCD evolution of two data sets were examined. First, only the parity-violating structure function xF_3 was used. The advantage of this method is that the evolution of xF_3 is independent of the gluon distribution. Second, a combined xF_3 and F_2 fit to the data was done. This increases the statistical power of the fit, but introduces extra parameters to describe the gluon distribution.

The QCD fits require initial parametrizations of the parton distributions at some Q_0^2. The forms used in this analysis were:

$$\begin{aligned} xq_{NS}(x,Q_0^2) &= A_{NS}x^{\eta_1}(1-x)^{\eta_2} && (23)\\ xq_S(x,Q_0^2) &= xq_{NS}(x,Q_0^2)+A_S(1-x)^{\eta_S} && (24)\\ xG(x,Q_0^2) &= A_G(1-x)^{\eta_G}, && (25) \end{aligned}$$

where NS and S refer to nonsinglet and singlet, respectively. Because this is a next-to-leading-order analysis, the fermion conservation rule, $\int_0^1 q_{NS}dx = 3$, is modified by a term proportional to $(1-\alpha_s/\pi)$ at next-to-leading order.[21] Also, there is a possible nuclear dependence which could lead to a violation of the fermion conservation rule by approximately 1%. Therefore, for this analysis, the fermion conservation rule was not required. The momentum sum rule, $\int_0^1(xq(x,Q_0^2)+xG(x,Q_0^2))dx = 1$, is not used to constrain A_G because the gluon distribution is unknown at low x. More complicated parametrizations of the parton distributions were found to have fit results consistent with the parametrizations above.[5] Parameterizations of target mass and higher twist effects, as described in Sec. 2.3 above, were included in the fitting procedure. The results of this fit were shown by the solid line on Figs. 5 and 6. The dashed lines on these figures represent an extrapolation of the parametrization from the global fit to lower Q^2 values.

The data were fit using MINUIT to minimize the χ^2 between the NLO QCD prediction and the data. Fits were for data with $Q^2 > 5$ GeV^2, $W^2 > 10$ GeV^2, and $x < 0.7$. Bins with statistical errors greater than 50% were eliminated. Positive and negative shifts of F_2 and xF_3 were made for each systematic error,

	$\Lambda_{\overline{MS}}^{NLO\ 4flv}$ from xF_3 only		$\Lambda_{\overline{MS}}^{NLO\ 4flv}$ from xF_3 and F_2	
Fit Type:	$\Lambda\pm$ stat $\pm$ sys	χ^2/DOF	$\Lambda\pm$ stat $\pm$ sys	χ^2/DOF
Basic	$336 \pm 41 \pm 84$	82/82	$346 \pm 21 \pm 54$	187/164
Global	$327 \pm 40 \pm 30$	75/82	$309 \pm 19 \pm 15$	167/164

Table 1: Preliminary values of $\Lambda_{\overline{MS}}^{NLO\ 4flv}$ determined from fits to the CCFR data.

and Λ was extracted. For this procedure, the χ^2 can be used to test the validity of QCD to describe the data. The theoretical prediction is based on the Duke and Owens NLO QCD Evolution Program.[22] The results of this fit are listed in Table 1, referred to as "basic." As expected, the fit which uses both the xF_3 and F_2 data have lower statistical and systematic errors because of the increased number of data points in the fit. The good χ^2/DOF indicates that the data are consistent with QCD.

An alternative fit procedure finds the best parameters to describe the data assuming that QCD is valid. For this analysis, a χ^2 fit to the theoretical prediction for the structure functions is compared to the data in each x and Q^2 bin. The prediction from the Duke and Owens program is compared to the data using a χ^2 that includes both statistical and systematic uncertainties with correlations. The systematic uncertainties are handled by introducing a parameter δ_k for each uncertainty k into the χ^2. Defining the structure function vector $F = (F_2\ xF_3)$ and the structure function error matrix $V = (\sigma_{ij})$, for $i, j = F_2, xF_3$, then the difference between the theoretical prediction and data and the χ^2 are:

$$F^{diff} = F^{data} - F^{theory} + \textstyle\sum_k \delta_k (F^k - F^{data}) \quad (26)$$

$$\chi^2 = (F^{diff}) V^{-1} (F^{diff})^T + \textstyle\sum_k \delta_k^2. \quad (27)$$

The results of this fit are listed under "global" in Table 1. The global fit gives a more precise measure of Λ because of the constraint of QCD.

The value of Λ from the global fit using F_2 and xF_3 is equivalent to $\alpha_s(M_Z^2) = 0.117 \pm 0.002(exp) \pm 0.004(theory)$. The theoretical error is due to the renormalization and factorization scale uncertainties.[8] This result is higher than the previous measurement of CCFR: $\alpha_s(M_Z^2) = 0.111 \pm 0.005$. It is also higher than the muon deep inelastic scattering result: $\alpha_s(M_Z^2) = 0.113 \pm 0.005$ (Ref. 23). It is lower than the LEP measurement from event shapes of 0.122 ± 0.007 (REf.[23]). How-

10bp

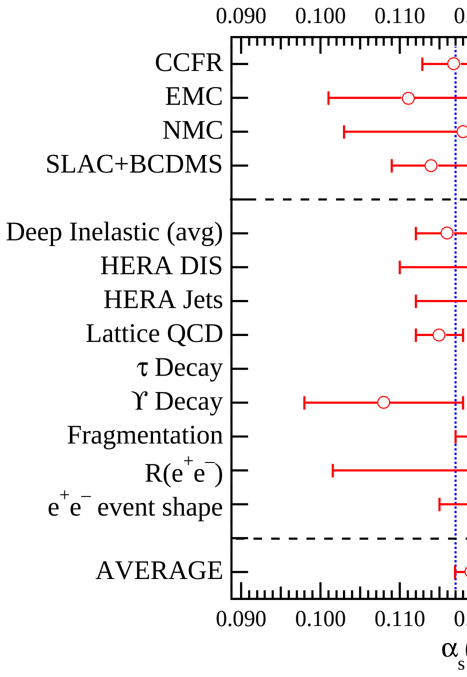

Figure 15: Measurement of α_s from various experiments. The CCFR result is preliminary. Results from other experiments are from Ref. 23.

ever, all of the above results are consistent within the errors. Figure 15 compares the preliminary CCFR result to results from other experiments.[23]

In the future, several improvements to the measurement of α_s are expected from CCFR/NuTeV. Using the method described above, the NuTeV experiment will make a more precise measurement of α_s by reducing the systematic errors associated with the measurement of the structure functions. A second method of measuring α_s, using the QCD corrections to the Gross-Llewellyn-Smith sum rule,[21] based on the new CCFR results, is also expected in the near future. This analysis extracts α_s at various Q^2 values in the low Q^2 region.[24]

6.3 Extraction of the Gluon Distribution

Fits to xF_3 and F_2, described above, allow one to extract the form of the gluon distribution. The global fit yields the preliminary distribution: $xG(x, Q_0^2 = 5GeV^2) = (2.34 \pm 0.36)(1-x)^{5.02\pm0.71}$.

Figure 16 shows this distribution as a function of x, evolved to $Q^2 = 32\ GeV^2$. The shaded region indicates the CCFR $\pm 1\sigma$ errors. For comparison, the crosses

10bp !

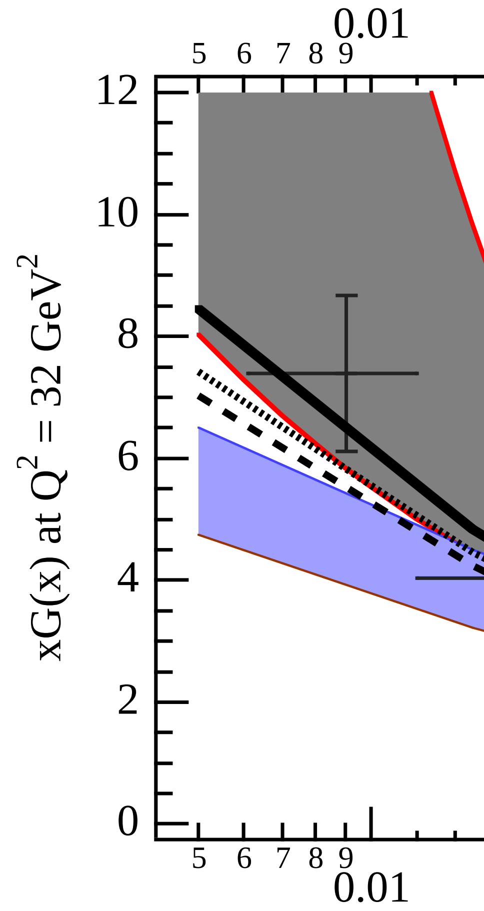

Figure 16: The CCFR gluon distribution evolved to $Q^2 = 32\ GeV^2$. Shaded region shows ±1σ errors. Crosses show results from HERA jet measurements. Dotted line is CTEQ4M. Solid line is GRV94 HO. Dashed line is MRS R2. Hatched region is gluon distribution from E665 hadronic energy distributions.

show the gluon distribution as measured from jet production at the H1 experiment.[25] The hatched region indicates the E665 gluon distribution measured from the energy distribution of hadrons produced in deep inelastic muon scattering.[3] Also shown are the gluon distributions from fits to data from a wide range of high-energy experiments which are available as parton distribution functions: CTEQ4M (Ref. 26) (dotted), GRV 94 HO (Ref. 27) (solid), and MRS R2 (Ref. 28) (dashed). The gluon distributions from the various experiments agree for the region of $x > 0.01$, the region of the CCFR data.

7 Conclusion

This paper has summarized the re-analysis of the CCFR data, resulting in preliminary new measurements of F_2 and xF_3. Comparisons of F_2 to charged lepton experiments indicate that there may be a discrepancy at low x after quark charge and nuclear corrections are applied. At present, this difference is not understood. The Q^2 evolution of these structure functions agrees with QCD and yields $\Lambda_{\overline{MS}}^{NLO\ 4flv} = 309 \pm 27(exp)\ MeV$. This is equivalent to $\alpha_s(M_Z^2) = 0.117 \pm 0.002(exp) \pm 0.004(theory)$.

References

[1] Adams *et al.*, Phys. Rev D **54**, 3006 (1996).

[2] Adams *et al.*, Phys. Rev. Lett. **75**, 1466 (1995).

[3] Adams *et al.*, Z. Phys. C **71**, 391 (1996).

[4] U. K. Yang *et al.*, J. Phys G **22**, 775 (1996).

[5] W. G. Seligman, *A Next-to-Leading-Order QCD Analysis of Neutrino–Iron Structure Functions at the Tevatron,* Columbia University Thesis, CU-398, Nevis report: Nevis-292.

[6] G. Altarelli *et al.*, Nucl. Phys. B 126, 298 (1977); Dokshitser *et al.*, Phys. Lett. B **78**, 290 (1978); Dokshitser *et al.*, Phys. Rep. **58**, 269 (1980); Gibov *et al.*, Sov. J. Nucl. Phys. **15**, 438 (1972).

[7] Georgi and Politzer Phys. Rev. D **14**, 1829 (1976).

[8] Virchaux *et al.*, Phys. Lett. B **274**, 221 (1992).

[9] Bazarko *et al.*, Z. Phys. C**65**, 189 (1995).

[10] Sakamoto *et. al.*, Nuc. Instrum. Methods A **294**, 179 (1990).

[11] R. Bernstein *et al.*, Fermilab TM-1884, 1994.

[12] Bardin *et al.*, JINR-ER-86-260 (1986).

[13] Whitlow *et al.*, Phys. Lett. B **282**, 475 (1992).

[14] Quintas, *Nucleon Structure Functions at the Fermilab Tevatron,* Columbia University Thesis, Nevis Preprint 277 (1992); Quintas *et al.*, Phys. Rev. Lett. **71**, 1307 (1993).

[15] Amaudruz *et al.*, Z. Phys. C **51**, 387 (1991).

[16] Amaudruz *et al.*, Phys. Lett. B **295**, 159 (1992).

[17] Allport *et al.*, Phys. Lett. B **232**, 417 (1989).

[18] Barone *et al.*, Phys. Lett. B **328**, 143 (1994).

[19] Botts *et al.*, Phys. Lett. B **304**, 159 (1993).

[20] Brodsky *et al.*, Phys. Lett. B **381**, 317 (1996).

[21] Gross *et al.*, Nucl. Phys. B **14**, 337 (1969).

[22] Devoto *et al.*, Phys. Rev. D **27**, 508 (1983).

[23] Barnett *et al.*, Phys. Rev. D **54** (1996).

[24] Harris *et al.*, FERMILAB-CONF-95-144, *Proc. of the 30th Renc. de Mor.* (1995).

[25] Aid *et al.*, Nucl. Phys. B **449**, 3 (1995).

[26] Lai *et al.*, MSUHEP-60426.

[27] Gluck *et al.*, Z. Phys. C. **67**, 433 (1995).

[28] Martin *et al.*, DTP/96/44, RAL-TR-96-037 (1996).